Spin Hall Magnetoresistance as a Probe for Surface Magnetization in Pt/CoFe$_2$O$_4$ Bilayers

Miren Isasa,[1] Saül Vélez,[1] Edurne Sagasta,[1] Amilcar Bedoya-Pinto,[1] Nico Dix,[2] Florencio Sánchez,[2] Luis E. Hueso,[1,3] Josep Fontcuberta,[2] and Fèlix Casanova[1,3]

[1]*CIC nanoGUNE, 20018 Donostia-San Sebastian, Basque Country, Spain*
[2]*Institut de Ciència de Materials de Barcelona (ICMAB-CSIC),*
Campus UAB, 08193 Bellaterra, Catalonia, Spain
[3]*IKERBASQUE, Basque Foundation for Science, 48013 Bilbao, Basque Country, Spain*

We study the spin Hall magnetoresistance (SMR) in Pt grown *in situ* on CoFe$_2$O$_4$ (CFO) ferrimagnetic insulating films. A careful analysis of the angle-dependent and field-dependent longitudinal magnetoresistance indicates that the SMR contains a contribution that does not follow the bulk magnetization of CFO, but it is a fingerprint of the complex magnetism at the surface of the CFO layer, thus signaling SMR as a tool for mapping surface magnetization. A systematic study of the SMR for different temperatures and CFO thicknesses gives us information impossible to obtain with any standard magnetometry technique. On one hand, the surface magnetization behaves independently of the CFO thickness and does not saturate up to high fields, evidencing that the surface has its own anisotropy. On the other hand, characteristic zero-field magnetization steps are not present at the surface while they are relevant in the bulk, strongly suggesting that antiphase boundaries are responsible for such intriguing features. In addition, a contribution from the ordinary magnetoresistance of Pt is identified, which is distinguishable only due to the low resistivity of the *in situ* grown Pt.

I. INTRODUCTION

Spin orbitronics is an emerging field in spintronics which exploits the strong spin-orbit coupling (SOC) present in nonmagnetic (NM) metals and semiconductors for the generation, manipulation, and detection of pure spin currents [1]. Many different phenomena arising from SOC, such as magnetic Skyrmions [2–4], the Rashba and Dresselhaus effects [5–7], the spin Hall effect (SHE) [8,9], or the spin-orbit torques for magnetic switching of ferromagnetic elements [10,11], are intensively being explored. Of particular interest is the SHE, a phenomenon in which an unpolarized charge current flowing through a NM metal with strong SOC is converted into a transverse spin current due to the opposite scattering of spin-up and spin-down electrons [8,9]. According to Onsager's reciprocity relations, a spin current flowing through a NM metal with strong SOC will in turn create a transverse charge current, known as the inverse SHE (ISHE). Extensive work has been carried out to quantify the strength of the effect in different metals [12–20].

Recently, a magnetoresistance that combines the SHE and ISHE has been discovered: the spin Hall magnetoresistance (SMR) [21–27]. This effect appears in bilayers formed by a NM metal with a strong SOC and a ferromagnetic insulator (FMI). Nakayama and co-workers [22] observed that, depending on the magnetization direction of the FMI, the spin current created by the SHE on the NM could be absorbed, *via* spin-transfer torque, or reflected at the NM/FMI interface, leading to a resistance

change in the NM. Given the interfacial origin of the effect, controlling the quality of the NM/FMI interface is crucial to get an enhanced magnetoresistance effect [27,28]. Although only recently discovered, the SMR has already proven to be a successful approach to quantify the spin-mixing interfacial conductance of NM/FMI bilayers [24–29], a concept at the base of this and other spin-dependent phenomena such as the spin Seebeck effect [29–32], spin pumping [17,18,20,29,33–35], or the magnetic gating of pure spin currents [36,37].

In this work, we demonstrate a functionality of the SMR by sensing the surface magnetization of the FMI. For this purpose, we choose CoFe$_2$O$_4$ (CFO), a room-temperature ferrimagnetic insulating oxide whose surface magnetization differs from that of the bulk due to its complex atomic constitution, competing magnetic interactions, and symmetry breaking [38,39]. The presence of Co^{2+} ions in its cubic spinel structure, (Fe^{3+})[Co^{2+}Fe^{3+}]O$_4$, anticipates a large magnetic anisotropy in CFO [38], and the competing nature of magnetic interactions in spinels may lead to different magnetic properties at the surface [39]. As the NM metal, we choose Pt, the most commonly used metal in experiments involving the spin-mixing conductance of NM/FMI bilayers [22–35]. In order to obtain clean Pt/CFO interfaces, Pt and CFO layers are grown *in situ*, in a single process, without air exposure between Pt and CFO layer deposition. We report magnetoresistance measurements, displaying features fully compatible with SMR, but with an additional signal arising from the ordinary

magnetoresistance (OMR) of Pt. This is made distinguishable by *in situ* growth of the bilayer. More importantly, by studying the field dependence of the longitudinal magnetoresistance arising from SMR, we are able to resolve the distinct surface-magnetization behavior of the CFO films, compared to its bulk magnetization.

II. EXPERIMENTAL DETAILS

A first set of three 40-nm-thick CFO films are epitaxially grown on (001) SrTiO₃ (STO) substrates by pulsed laser deposition. The beam of a KrF excimer laser is focused on a CFO target at an angle of 45°. The fluence and repetition rate are 1.5(3) J/cm² and 5 Hz, respectively. The substrate temperature is about 550 °C and oxygen pressure $P_{O2} =$ 0.1 mbar [40]. Crucial for the SMR phenomenon is the nature of the interface between the FMI and the NM (Pt in the present case) layers [23,27,28,41–43]. As shown in a previous work [27], the magnitude of the SMR strongly depends on the interface preparation conditions, being optimal when the NM is grown *in situ* on top of the FMI. For this reason, Pt with three different thicknesses ($t_{Pt} =$ 6.5, 4, and 2 nm) is epitaxially grown by dc sputtering on CFO by an *in situ* process at 400 °C. The thicknesses of the CFO and Pt layers are inferred from growth-rate calibration by x-ray reflectometry. $\theta/2\theta$ scans are used to confirm that all CFO films are fully (001) textured without a spurious phase and that Pt layers are also (001) textured. For transport measurements, the Pt layers are patterned into Hall bars (width $W = 100$ μm and length $L = 800$ μm), as sketched in Fig. 1, using electron-beam lithography with a negative resist on top of the Pt layer,

followed by Ar-ion milling and lift-off. The longitudinal base resistances (R_{L0}) of the 6.5-, 4-, and 2-nm-thick Pt films are 272 (144) Ω, 403 (364) Ω, and 1440 (1198) Ω, respectively, yielding resistivities of 21.5 (11.4), 20.2 (17.7), and 36.0 (30.0) $\mu\Omega$ cm at 300 (50) K.

A second set of four samples is fabricated in the same way. For this set, 20-, 30-, 40-, and 60-nm-thick CFO films are grown, whereas the Pt thickness is fixed to 2 nm.

Magnetization and magnetotransport measurements are performed in the same liquid-He cryostat, where the temperature varies from 300 to 40 K with externally applied magnetic fields (**H**) ranging from −9 to 9 T. Vibrating sample magnetometry (VSM) is used to determine the magnetization of the CFO films. Transport measurements are performed using a Keithley 6221 sourcemeter and a Keithley 2182 A nanovoltmeter operating in the dc-reversal method [44] with 100 μA of applied current. Field-dependent magnetoresistance (FDMR) measurements are carried out in the longitudinal configuration, as sketched in Fig. 1, where the field is applied in three different directions: (i) along the current direction (**j** direction), (ii) in plane and transverse to **j** (**t** direction), and (iii) out of plane (**n** direction). Angle-dependent magnetoresistance (ADMR) measurements are also performed in the longitudinal configuration, in which the applied field is fixed at 9 T and varies along the different **H**-rotation planes. Their corresponding angles are defined as (i) α (from **j**, angle $\alpha = 0$, towards **t**), (ii) β (from **n**, angle $\beta = 0$, towards **t**), and (iii) γ (from **n**, angle $\gamma = 0$, towards **j**). All these **H**-rotation planes are schematically shown in Fig. 1.

III. RESULTS AND DISCUSSION

A. Angle-dependent magnetoresistance measurements

According to the SMR theory, the angular dependence of the measured longitudinal (ρ_L) and transverse (ρ_T) resistivity is given by [21]

$$\rho_L = \rho_0 + \Delta\rho_1(1 - m_t^2), \tag{1}$$

$$\rho_T = \Delta\rho_1 m_j m_t + \Delta\rho_2 m_n, \tag{2}$$

where ρ_0 is the baseline resistivity of the NM layer, the ratio $\Delta\rho_1/\rho_0$ is the SMR, and $\Delta\rho_2$ accounts for an anomalous Hall-like contribution. $\mathbf{m}(m_j, m_t, m_n) = \mathbf{M}/M_s$ are the cosine directors of the magnetization **M** along the **j**, **t**, and **n** directions. M_s is the saturation magnetization of CFO. In Fig. 1, we show the measured ADMR of the Pt(6.5 nm)/CFO(40 nm) sample at 300 K, defined by their corresponding angles α, β, and γ. All the measurements are performed in the longitudinal configuration at fields $\mu_0 H$ (9 T) much larger than the coercive field $\mu_0 H_c$ of the CFO [see Fig. 5(a)]. Hence, we initially assume that, in Fig. 1, **m** roughly follows **H**. Transverse ADMR measurements as a function of angle α yield the same amplitude
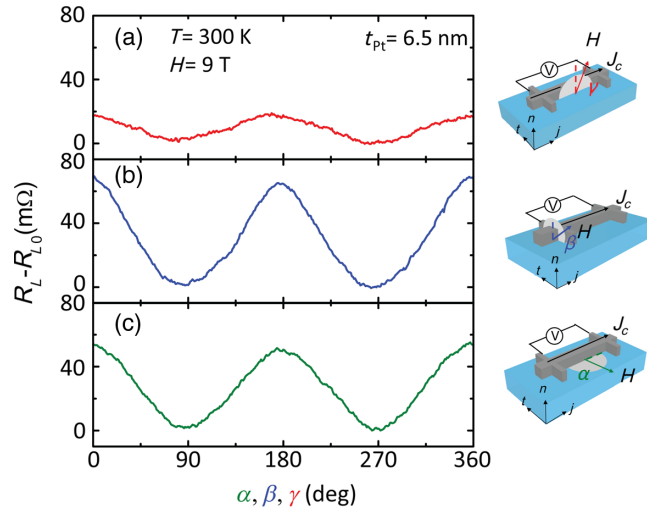

FIG. 1. Angle-dependent magnetoresistance measurements at 9 T and 300 K for the Pt(6.5 nm)/CFO(40 nm) sample along (a) γ, (b) β, and (c) α rotation planes. R_L is the measured longitudinal resistance and R_{L0} the subtracted background. The sketches in the right define the Hall bar geometry, the longitudinal measurement setup, and the angles α, β, and γ.

($\Delta\rho_1$) as the longitudinal measurements [27], whereas the term $\Delta\rho_2$ is completely hidden by the ordinary Hall effect of Pt when **H** is rotated in the β and γ planes [25]. Since these measurements do not give additional information, they are not shown for the sake of simplicity.

Based on the SMR scenario, the longitudinal resistance R_L of Pt should change only when the direction of the magnetization changes with respect to the spin polarization **s**, which points to **t** direction due to the symmetry of the SHE [22]. Thus, a change in resistance should appear only when the field is rotated along α and β angles. The measured resistance follows $R_L(\alpha) \propto \cos^2(\alpha)$ and $R_L(\beta) \propto \cos^2(\beta)$, respectively, and the magnetoresistance value should be similar in both cases, $\Delta R(\beta) = \Delta R(\alpha)$. Additionally, $R_L(\gamma)$ should not vary when **H** is rotated along γ, as in this case **M** is always perpendicular to **s**, and so $m_t = 0$. However, the measurements in Fig. 1 reveal a different scenario. On the one hand, $R_L(\gamma)$ is not a constant value when rotating **H** [Fig. 1(a)]. On the other hand, the change in $R_L(\beta)$ [Fig. 1(b)] is different from the change in $R_L(\alpha)$ [Fig. 1(c)]. In fact, the difference between both curves [$R_L(\alpha)$ and $R_L(\beta)$] yields the same modulation observed in $R_L(\gamma)$. A very controversial issue when placing the Pt next to a FMI is the magnetization that can be induced in Pt by the proximity effect, since Pt is close to the Stoner ferromagnetic instability [45–48]. If this was the case, $R_L(\gamma)$ measurements, which follow $R_L(\gamma) \propto \cos^2(\gamma)$, could be a signature of the anisotropic magnetoresistance (AMR) of the magnetized Pt. As AMR is sensitive to the variation of the magnetization with respect to the charge-current direction, it would also be contributing to the $R_L(\alpha)$ measurements, this configuration being sensitive to both AMR and SMR.

To further understand the modulation that we observe in $R_L(\gamma)$, we perform the same measurements for samples with different Pt thicknesses and at different temperatures, ranging from 40 to 300 K (Fig. 2). As observed, the normalized magnetoresistance in $R_L(\gamma)$, $\Delta R(\gamma)/R_{L0}$, is present for different Pt thicknesses and for all temperatures, being largest for the case of the thickest Pt. The fact that this contribution decreases when reducing thickness rules out that it arises from a proximity effect which should be more relevant for thinner films [49]. Additionally, Fig. 2 shows that $\Delta R(\beta)/R_{L0}$, the purely SMR signal, becomes more important at low thicknesses, as expected [23,25,27].

B. Field-dependent magnetoresistance measurements

Another strategy to rule out the possibility of having AMR in a magnetized Pt is performing FDMR measurements fixing the direction of the magnetic field (**n**, **t**, or **j**) and sweeping it from −9 to 9 T (see Fig. 3). If AMR is present in our samples, we should obtain the distinct trend of the magnetoresistance when the field is applied perpendicular to the charge current (**H**||**t** and **H**||**n**) and when it is applied parallel to the charge current (**H**||**j**).
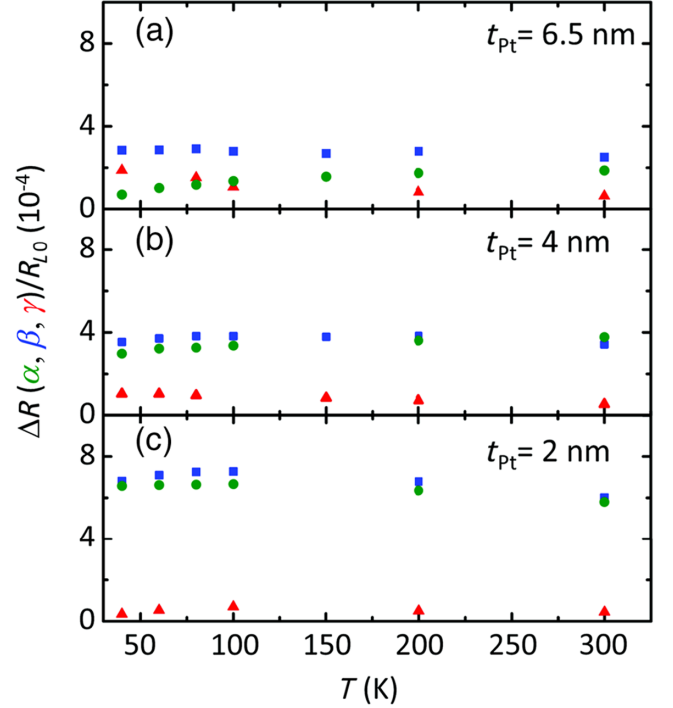

FIG. 2. The amplitude of ADMR at 9 T as a function of the temperature, for the three different angles α (green circles), β (blue squares), and γ (red triangles), for (a) Pt(6.5 nm)/CFO(40 nm), (b) Pt(4 nm)/CFO(40 nm), and (c) Pt(2 nm)/CFO(40 nm) samples.

However, this is not what Fig. 3 shows, since the **H**||**n** curves have the same magnetoresistance trend as the **H**||**j** curves and opposite to the one observed with **H**||**t**, irrespective of the Pt thickness. Therefore, the AMR contribution should be discarded. This conclusion is in agreement with recent atomic selective magnetic measurements in similar Pt/CFO layers where, within the experimental resolution, no magnetic moment has been found at the Pt [50].

It is worth noting the different resistance values measured for **H**||**j** and **H**||**n** at high fields, which accounts for the modulation in $R_L(\gamma)$, and it strongly depends on the Pt thickness, being more pronounced for the thickest sample. A possible explanation for this behavior is related to the OMR in Pt. This magnetoresistance effect appears in metals and semiconductors, and it occurs because conduction electrons are displaced from their trajectories by the Lorentz force exerted by an externally applied magnetic field. The magnetoresistance due to the OMR ($\Delta R_{OMR}/R_{L0}$) can be described by the Kohler's rule, which depends on the applied field and resistivity in the form of [51,52]

$$\frac{\Delta R_{OMR}}{R_{L0}} = a\left(\frac{H}{\rho}\right)^n, \quad (3)$$
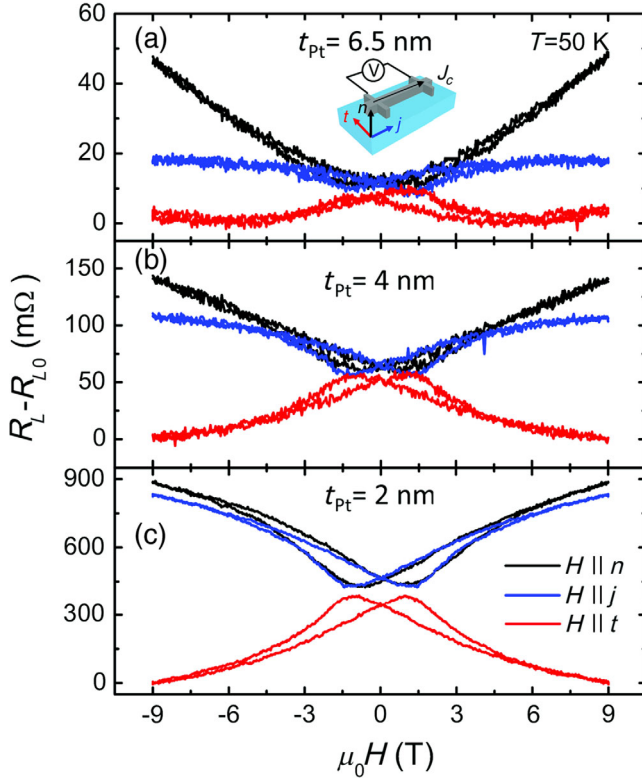
FIG. 3. Longitudinal resistance R_L for (a) Pt(6.5 nm)/CFO(40 nm), (b) Pt(4 nm)/CFO(40 nm), and (c) Pt(2 nm)/CFO(40 nm) samples, as a function of H applied along **t** (red curves), **j** (blue curves), and **n** (black curves). R_{L0} is the subtracted background. The orientations of the applied field and the measurement configuration are sketched in the inset. All measurements are done at 50 K.

FIG. 4. Orange, blue, and green curves are the additional magnetoresistance observed for out-of-plane H, $[R_L(\mathbf{H}||\mathbf{n})-R_L(\mathbf{H}||\mathbf{j})]/R_{L0}$, as a function of H/ρ for the three Pt/CFO(40 nm) samples with different Pt thicknesses at 50 K. The red curve is the longitudinal magnetoresistance $[R_L(\gamma)-R_{L0}]/R_{L0}$ as a function of $H\cos(\gamma)/\rho$, where $H\cos(\gamma)$ is the out-of-plane component of the field for the 6.5-nm-thick Pt, at 300 K. The dashed black line is a guide for the eye.

where a and n are material-dependent constants, with n between 1 and 2. This magnetoresistance should be characteristic of the Pt but independent of the Pt thickness, as far as its scattering length is not affected by size effects. To verify this, we subtract $R_L(\mathbf{H}||\mathbf{n}) - R_L(\mathbf{H}||\mathbf{j})$ to obtain ΔR and normalize it to R_{L0}, which should correspond to the extra magnetoresistance present in the system. Subsequently, we plot the extra magnetoresistance as a function of H/ρ (see Fig. 4). As expected, all data define a parabolalike curve, with $n = 1.8$, confirming that this extra effect is OMR. OMR has not been detected in previous studies on Pt/FMI [25,53], due the large resistivity usually obtained in Pt thin films (approximately 41–60 $\mu\Omega$ cm). Our Pt, grown *in situ* at 400 °C on top of epitaxial (001) CFO, is fully textured in the (001) direction, leading to a lower resistivity and therefore to a non-negligible OMR contribution.

Note that, once the OMR contribution is identified in $R_L(\mathbf{H}||\mathbf{n})$, the curves arising solely from the SMR contribution are $R_L(\mathbf{H}||\mathbf{t})$ and $R_L(\mathbf{H}||\mathbf{j})$. As expected (Fig. 3), the curves show a mirror symmetry and have the same
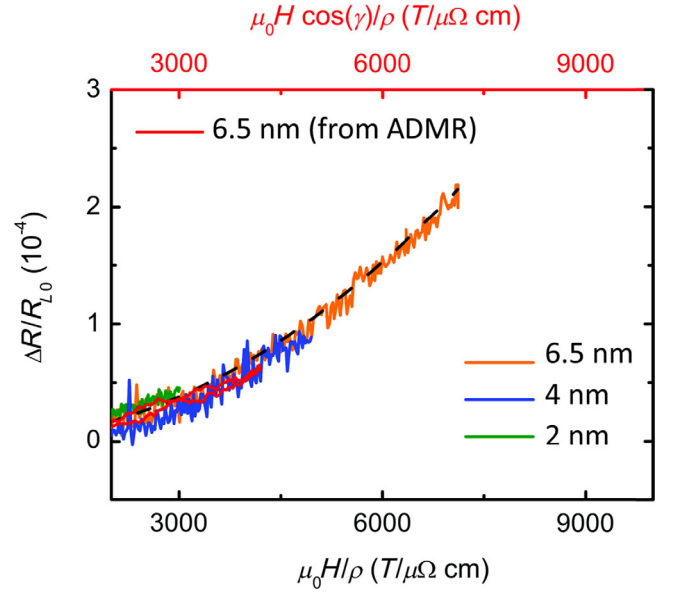
shape with the Pt thickness, and the SMR magnitude decreases with increasing thickness [23,25,27].

Now we can safely ascribe the behavior observed in Fig. 1(a) to OMR, where the angular dependence comes from the out-of-plane component of the field [$H\cos(\gamma)$]. If we plot the measured $R_L(\gamma)$ as a function of $H\cos(\gamma)/\rho$, we can see that it nicely follows Kohler's curve (red curve in Fig. 4). Note that the curves in Fig. 4 correspond to different temperatures: FDMR measurements are done at 50 K and ADMR at 300 K. The fact that they all lie over the same curve is clear evidence that OMR is temperature independent.

C. Comparison between VSM and SMR measurements

Once we identify the coexistence of SMR and OMR in our system, we move now to the comparison between the magnetic properties of the CFO thin films and the spin Hall magnetoresistance of the Pt/CFO bilayers. Figure 5(a) shows the hysteresis loops $M(H)$ of the Pt(2 nm)/CFO(40 nm) sample obtained by VSM when applying the magnetic field **H** along the **t** and **n** directions at 50 K. As can be seen from the hysteresis loop when the field is applied in plane, $M(\mathbf{H}||\mathbf{t})$, the large coercive fields $\mu_0 H_c(\mathbf{t}) \approx \pm 1.2$ T and the fact that hysteresis disappears only at approximately 5 T are signatures of the strong magnetic anisotropy typical of CFO thin films [54,55]. The shape of the hysteresis loop when the field is applied out of plane, $M(\mathbf{H}||\mathbf{n})$, indicates a harder
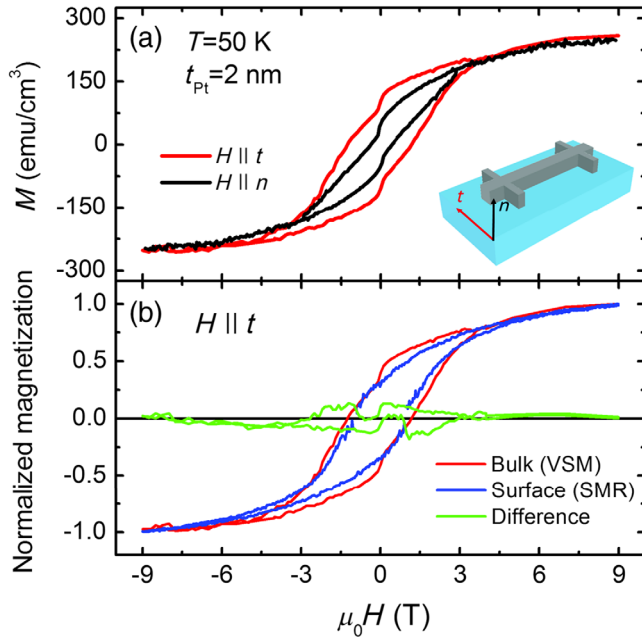
FIG. 5. (a) Magnetic hysteresis loops for the Pt(2 nm)/CFO(40 nm) sample measured by VSM at 50 K. H is applied along $\mathbf{t}$ (red curve) and $\mathbf{n}$ (black curve), as defined in the inset. A diamagnetic background has been subtracted. (b) Comparison of normalized hysteresis loops with H applied along $\mathbf{t}$ for the same sample. The red curve is the one in (a), normalized to the maximum value. The blue curve is computed from the longitudinal resistance R_L at 50 K as a function of H applied along $\mathbf{t}$, which is shown in Fig. 3(c). The green curve is the difference between the two hysteresis loops.

magnetization axis, and, correspondingly, the coercive field $\mu_0 H_c(\mathbf{n}) \approx \pm 0.44$ T and the magnetic remanence are smaller. The saturation magnetization ($M_s = 230$ emu/cm³) is lower than the corresponding bulk value as commonly observed in spinel thin films [56–59] and attributed to the presence of antiphase boundaries (APBs) [56,57] or to surface anisotropy effects [39]. Characteristic steps are observed in the hysteresis loops around zero field. These steplike features are commonly found in CFO thin films [54,60] and other ferrimagnetic oxides such as Fe_3O_4 [57] or $\varepsilon\text{-}Fe_2O_3$ [61] and were attributed to the result of coupled antiferromagnetic domains due to the presence of APBs by Sofin, Arora, and Shvets [62]. A larger density of APBs would lead to a larger step at zero field. The diamagnetic background, arising mainly from the STO substrate, is corrected by subtracting a linear term $\chi_d H$, where χ_d is the high-field slope of the raw data. The χ_d values are practically identical for all $\mathbf{H}$ orientations, as expected for the cubic STO substrate (not shown). Note that the presence of such a background, however, would conceal any possible contribution from nonsaturating behavior of the CFO film at high fields, as commonly observed in these systems [54,59,60].

Figure 3(c) shows the longitudinal resistance of the Pt(2 nm)/CFO(40 nm) sample measured at different

orthogonal $\mathbf{H}$ orientations [$R_L(\mathbf{H}\|\mathbf{j})$, $R_L(\mathbf{H}\|\mathbf{t})$, and $R_L(\mathbf{H}\|\mathbf{n})$], after subtracting the background resistance. When applying a field $\mathbf{H}\|\mathbf{n}$, the transverse component of the magnetization m_t should be reduced, and, following Eq. (1), $R_L(\mathbf{H}\|\mathbf{n})$ should increase with H. A similar behavior is expected for $R_L(\mathbf{H}\|\mathbf{j})$ when applying a field $\mathbf{H}\|\mathbf{j}$. Accordingly, $R_L(\mathbf{H}\|\mathbf{t})$ should decrease with increasing H. The experimental data in Fig. 3(c) confirm these trends. As expected, this behavior shares similarities and is reminiscent of the $M(H)$ curves in Fig. 5(a), because, as shown by Eq. (1), the field evolution of $M(H)$ should translate into $R_L(H)$. Taking into account that m_t in Eq. (1) is the cosine director of the magnetization $\mathbf{M}$ along the $\mathbf{t}$ direction [$m_t = \cos(\Psi)$], one could perform a more quantitative analysis by extracting the angle Ψ between $\mathbf{M}$ and $\mathbf{t}$ as a function of the applied magnetic field from $R_L(\mathbf{H}\|\mathbf{t})$. In particular, Eq. (1) can be rewritten as $(\rho_L - \rho_0)/\Delta\rho_1 = (1 - m_t^2) = \sin^2(\Psi)$. In order to normalize our magnetoresistance measurements in the same way, we assume that the local maxima R_{max} in the $R_L(\mathbf{H}\|\mathbf{t})$ curve [see Fig. 3(c)] corresponds to $\Psi = 90°$ and the value at the largest field (9 T) is saturated and corresponds to $\Psi = 0°$. These assumptions are not strictly correct, because (i) we do not know exactly how $\mathbf{M}$ rotates with $\mathbf{H}$ (we could have a Ψ lower than 90° in the local maxima) and (ii) $R_L(\mathbf{H}\|\mathbf{t})$ does not fully saturate at 9 T. With these precautions, we compute $[R_L(H)\text{-}R_L(9\text{ T})]/[R_{max}\text{-}R_L(9\text{ T})] \approx \sin^2(\Psi)$. From here, one can calculate $m_t = \cos(\Psi)$, which is also the $\mathbf{M}$ component measured in the VSM magnetometer when using the in-plane field configuration, as a function of the magnetic field. Note that the above analysis cannot be done for $R_L(\mathbf{H}\|\mathbf{j})$ and $R_L(\mathbf{H}\|\mathbf{n})$, because in those cases the other two components of $\mathbf{M}$ (m_n and m_j) cannot be univocally determined.

Figure 5(b) shows the resulting hysteresis loop (blue line). Superposed are the normalized $M(H)$ data obtained with VSM magnetometry along the $\mathbf{t}$ direction (red line). It is remarkable that the shape of the hysteresis loop extracted from the surface-sensitive SMR measurements is similar to the bulk-sensitive $M(H)$ loop, except for the characteristic steps observed around zero field in the $M(H)$ curve which are absent in $m_t(H)$. Accordingly, our semiquantitative analysis strongly suggests a reduced density of APBs at the surface of our CFO films, while APBs are present in the bulk. There is abundant literature indicating that the density of APBs in spinel oxide films (Fe_3O_4 [57] and CFO [63]) decreases as the films get thicker. On the basis of these results, it could be expected that the density of APBs also decreases when approaching the film surface. Indeed, APBs are defective regions generated essentially at the first layers during initial growth, and their presence unavoidably produces strain gradients in the films. Elastic energy shall be released during film growth, and the simplest way is to reduce the APB density away from the interface with the substrate. Within the scope of the

APB model developed by Sofin, Arora, and Shvets [62], the observed difference between bulk and surface magnetization [green line in Fig. 5(b)] would reflect the magnetization reversal of domains antiferromagnetically coupled across APBs.

From this comparison, we conclude that SMR is extremely sensitive to fine details of the magnetic ordering at the Pt/CFO interface and $R_L(H)$ data are thus fingerprints of a distinct surface magnetization which, although not discernible in the bulk-sensitive magnetization experiments, largely dominates the longitudinal SMR. A further systematic SMR study in CFO films with different thicknesses will help to understand the particular complexity of surface magnetization in spinel structures.

D. Surface magnetization as a function of CFO thickness

For this reason, we fabricate *ex professo* a set of Pt/CFO samples with a fixed Pt thickness of 2 nm (in order to maximize the SMR amplitude) and CFO thicknesses of 20, 30, 40, and 60 nm. We systematically measure hysteresis loops with VSM for all thicknesses at temperatures between 10 and 300 K [64]. As mentioned above, the approach to saturation critically depends on the protocol to subtract the diamagnetic background [64]. Most of the corrected hysteresis loops display a saturated behavior, as a linear contribution has been subtracted, but also some inconsistencies are present (see Fig. S1 and 7); i.e., information on a high field magnetic susceptibility is lost by this subtraction protocol, which thus invalidates any critical analysis of the approach to saturation. We also stress that, in this set of samples, the characteristic steps at zero field in the magnetization curves are observed clearly only for the thinnest (20 nm) CFO film (Fig. S1 and 7); this finding is fully consistent with the proposed inverse correlation between the APB density and film thickness.

FDMR is measured at several temperatures (50, 150, and 300 K) with the magnetic field applied in two relevant directions ($\mathbf{H}\|\mathbf{n}$ and $\mathbf{H}\|\mathbf{t}$). Figure 6 shows the results for two different CFO thicknesses (20 and 60 nm). The amplitudes of SMR are very similar to those observed in the Pt(2 nm)/CFO(40 nm) sample of the previous set [Fig. 2(c)].

We use the semiquantitative model described in the previous subsection to derive a normalized hysteresis loop for Pt(2 nm)/CFO(20 nm) and Pt(2 nm)/CFO(60 nm) samples at different temperatures. In Fig. 7, we show the comparison of the SMR hysteresis loops with the normalized hysteresis loops obtained by VSM. Two main features should be highlighted here. (i) In all cases, SMR hysteresis loops display a slow approach to saturation. We stress again that this information could not be conclusively assessed from the VSM hysteresis loops. (ii) The characteristic steps at zero field in the VSM loop for Pt(2 nm)/CFO(20 nm)
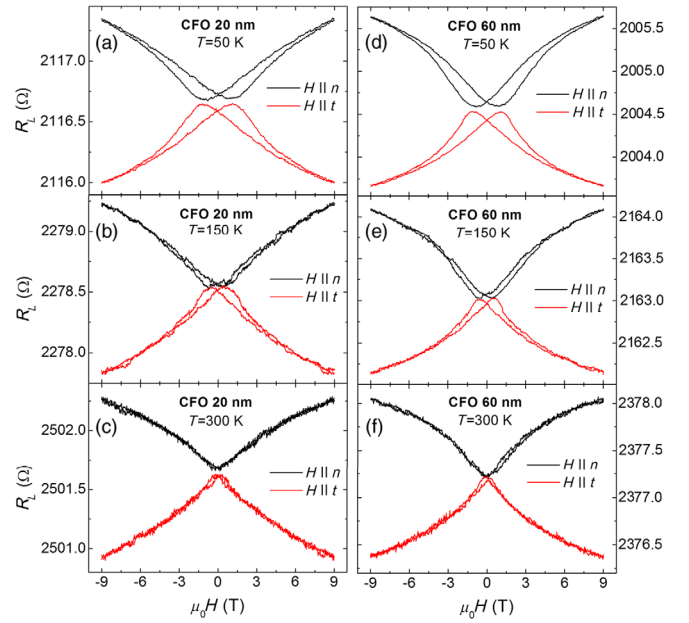

FIG. 6. Longitudinal resistance R_L for (a)–(c) Pt(2 nm)/CFO(20 nm) and (d)–(f) Pt(2 nm)/CFO(60 nm) samples, as a function of H applied along $\mathbf{t}$ (red curves) and $\mathbf{n}$ (black curves). Measurements are done at 50 (a),(d), 150 (b),(e), and 300 K (c),(f).

are not present in the corresponding SMR loop [Fig. 7(a)], confirming our previous observation from Fig. 5(b).

In Fig. 8, we plot SMR hysteresis loops for Pt(2 nm)/CFO(20 nm) and Pt(2 nm)/CFO(60 nm) samples at different temperatures. Surprisingly, the SMR hysteresis
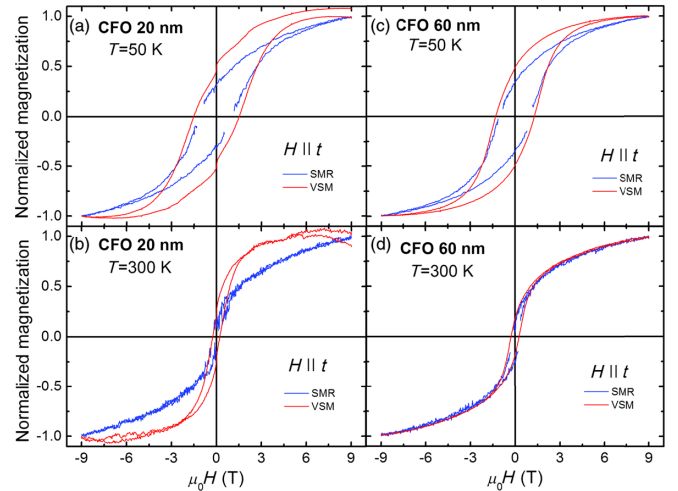

FIG. 7. Comparison of normalized magnetic hysteresis loops with H applied along $\mathbf{t}$ for (a),(b) Pt(2 nm)/CFO(20 nm) and (c),(d) Pt(2 nm)/CFO(60 nm) samples at 50 (a),(c) and 300 K (b),(d). The red curve is measured by VSM magnetometry and normalized to the maximum value after diamagnetic background subtraction. The blue curve is computed from the longitudinal resistance R_L as a function of H applied along $\mathbf{t}$, which is shown in Fig. 6.

loops are almost identical for 20- and 60-nm-thick CFO films at any temperature. This is not the case for the VSM hysteresis loops. This impressive result clearly indicates that the surface has the same magnetic behavior independently of the CFO film thickness, which is completely different from the bulk behavior, and highlights the importance of surface anisotropy.

In summary, this series of hysteresis loops derived from SMR for different temperatures and CFO thicknesses gives us consistent results on the complex magnetism of CFO,

impossible to obtain with any standard magnetometry technique: (i) The surface magnetization behaves independently of the CFO thickness and does not saturate up to 9 T, evidencing that the surface has its own anisotropy; (ii) the characteristic zero-field steps are not present at the surface magnetization while they are relevant in the bulk, strongly suggesting that APBs are responsible for such intriguing features.

IV. CONCLUSIONS

We report longitudinal magnetoresistance measurements of *in situ* grown Pt on ferrimagnetic insulating CFO, as a function of the intensity and orientation of the magnetic field. We show that, even if the data can be well described by the spin Hall magnetoresistance, an additional feature appears at high magnetic fields, which originates from the ordinary magnetoresistance of Pt. Furthermore, we compare the field-dependent longitudinal resistance arising from the SMR to the bulk magnetization of the CFO. This analysis reveals important differences that we correlate to the significant role of antiphase boundaries and surface anisotropy in systems such as spinels where strong competition of magnetic interactions takes place. The present work shows the tremendous potential of spin Hall magnetoresistance to probe the surface magnetization of magnetic insulators, otherwise not possible with standard magnetometric techniques.
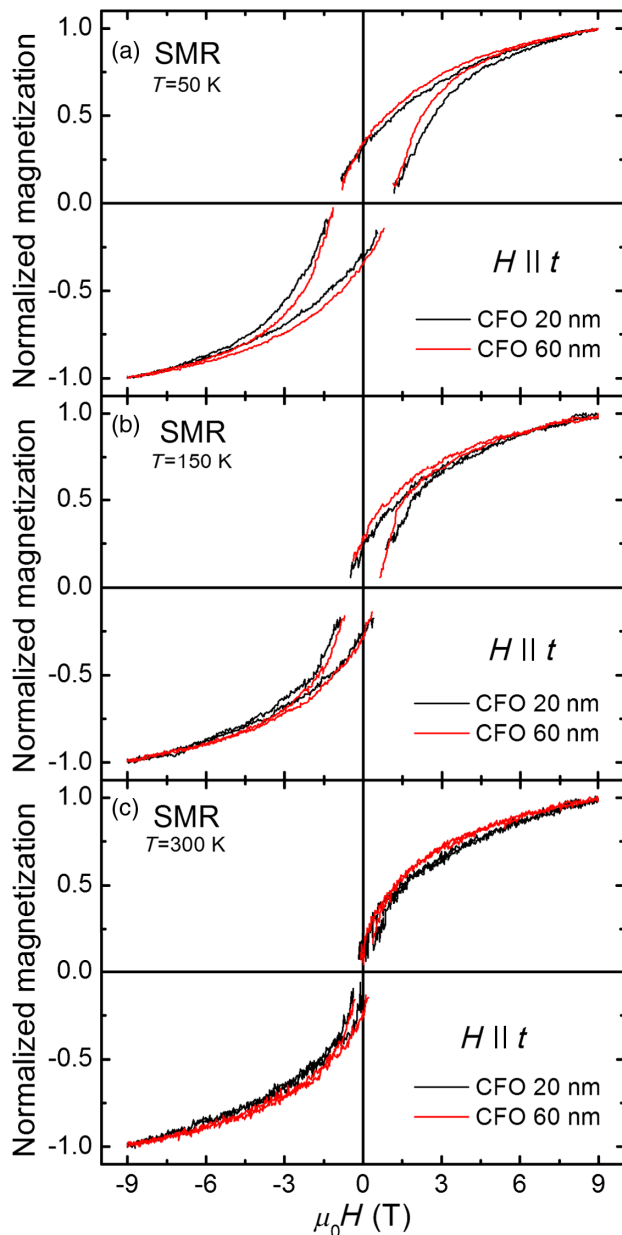
FIG. 8.   Comparison of normalized hysteresis loops for Pt(2 nm)/ CFO(20 nm) (black curves) and Pt(2 nm)/CFO(60 nm) (red curves) samples, computed from the longitudinal resistance R_L at (a) 50, (b) 150, and (c) 300 K, as a function of H applied along **t** (shown in Fig. 6).

[1] *Spin Current*, edited by S. Maekawa, S. O. Valenzuela, E. Saitoh, and T. Kimura (Oxford University Press, New York, 2012).

[2] S. Mühlbauer, B. Binz, F. Jonietz, C. Pfleiderer, A. Rosch, A. Neubauer, R. Georgii, and P. Böni, Skyrmion lattice in a chiral magnet, Science **323**, 915 (2009).

[3] N. Nagaosa and Y. Tokura, Topological properties and dynamics of magnetic Skyrmions, Nat. Nanotechnol. **8**, 899 (2013).

[4] A. Fert, V. Cros, and J. Sampaio, Skyrmions on the track, Nat. Nanotechnol. **8**, 152 (2013).

[5] J. C. Rojas Sánchez, L. Vila, G. Desfonds, S. Gambarelli, J. P. Attané, J. M. De Teresa, C. Magén, and A. Fert, Spin-to-charge conversion using Rashba coupling at the interface

between non-magnetic materials, Nat. Commun. **4**, 2944 (2013); S. Sangiao, J. M. De Teresa, L. Morellón, I. Lucas, M. C. Martínez-Velarte, and M. Viret, Control of the spin to charge conversion using the inverse Rashba-Edelstein effect, Appl. Phys. Lett. **106**, 172403 (2015).

[6] W. Zhang, M. B. Jungfleisch, W. Jiang, J. E. Pearson, and A. Hoffmann, Spin pumping and inverse Rashba-Edelstein effect in NiFe/Ag/Bi and NiFe/Ag/Sb, J. Appl. Phys. **117**, 17C727 (2015).

[7] M. Isasa, M. C. Martínez-Velarte, E. Villamor, C. Magén, L. Morellón, J. M. De Teresa, M. R. Ibarra, G. Vignale, E. V. Chulkov, E. E. Krasovskii, L. E. Hueso, and F. Casanova, Origin of inverse Rashba-Edelstein effect detected at the Cu/Bi interface using lateral spin valves, Phys. Rev. B **93**, 014420 (2016).

[8] M. I. Dyakonov and V. I. Perel, Current-induced spin orientation of electrons in semiconductors, Phys. Lett. **35A**, 459 (1971).

[9] J. E. Hirsch, Spin Hall Effect, Phys. Rev. Lett. **83**, 1834 (1999).

[10] I. M. Miron, K. Garello, G. Gaudin, P.-J. Zermatten, M. V. Costache, S. Auffret, S. Bandiera, B. Rodmacq, A. Schuhl, and P. Gambardella, Perpendicular switching of a single ferromagnetic layer induced by in-plane current injection, Nature (London) **476**, 189 (2011).

[11] L. Liu, C.-F. Pai, Y. Li, H. W. Tseng, D. C. Ralph, and R. A. Buhrman, Spin-torque switching with the giant spin Hall effect of tantalum, Science **336**, 555 (2012); C.-F. Pai, L. Liu, Y. Li, H. W. Tseng, D. C. Ralph, and R. A. Buhrman, Spin transfer torque devices utilizing the giant spin Hall effect of tungsten, Appl. Phys. Lett. **101**, 122404 (2012).

[12] S. Valenzuela and M. Tinkham, Direct electronic measurement of the spin Hall effect, Nature (London) **442**, 176 (2006).

[13] M. Morota, Y. Niimi, K. Ohnishi, D. H. Wei, T. Tanaka, H. Kontani, T. Kimura, and Y. Otani, Indication of intrinsic spin Hall effect in 4d and 5d transition metals, Phys. Rev. B **83**, 174405 (2011).

[14] Y. Niimi, H. Suzuki, Y. Kawanishi, Y. Omori, T. Valet, A. Fert, and Y. Otani, Extrinsic spin Hall effects measured with lateral spin valve structures, Phys. Rev. B **89**, 054401 (2014).

[15] M. Isasa, E. Villamor, L. E. Hueso, M. Gradhand, and F. Casanova, Temperature dependence of spin diffusion length and spin Hall angle in Au and Pt, Phys. Rev. B **91**, 024402 (2015); **92**, 019905(E) (2015).

[16] E. Sagasta, Y. Omori, M. Isasa, M. Gradhand, L. E. Hueso, Y. Niimi, Y. Otani, and F. Casanova, Tuning the spin Hall effect of Pt from the moderately dirty to the superclean regime, Phys. Rev. B **94**, 060412(R) (2016).

[17] A. Azevedo, L. H. Vilela-Leao, R. L. Rodriguez-Suarez, A. F. Lacerda Santos, and S. M. Rezende, Spin pumping and anisotropic magnetoresistance voltages in magnetic bilayers: Theory and experiment, Phys. Rev. B **83**, 144402 (2011).

[18] O. Mosendz, J. E. Pearson, F. Y. Fradin, G. E. W. Bauer, S. D. Bader, and A. Hoffmann, Quantifying Spin Hall Angles from Spin Pumping: Experiments and Theory, Phys. Rev. Lett. **104**, 046601 (2010).

[19] L. Liu, T. Moriyama, D. C. Ralph, and R. A. Buhrman, Spin-Torque Ferromagnetic Resonance Induced by the Spin Hall Effect, Phys. Rev. Lett. **106**, 036601 (2011).

[20] M. Obstbaum, M. Härtinger, H. G. Bauer, T. Meier, F. Swientek, C. H. Back, and G. Woltersdorf, Inverse spin Hall effect in Ni$_{81}$Fe$_{19}$/normal-metal bilayers, Phys. Rev. B **89**, 060407(R) (2014).

[21] Y.-T. Chen, S. Takahashi, H. Nakayama, M. Althammer, S. T. B. Goennenwein, E. Saitoh, and G. E. W. Bauer, Theory of spin Hall magnetoresistance, Phys. Rev. B **87**, 144411 (2013).

[22] H. Nakayama, M. Althammer, Y.-T. Chen, K. Uchida, Y. Kajiwara, D. Kikuchi, T. Ohtani, S. Geprägs, M. Opel, S. Takahashi, R. Gross, G. E. W. Bauer, S. T. B. Goennenwein, and E. Saitoh, Spin Hall Magnetoresistance Induced by a Nonequilibrium Proximity Effect, Phys. Rev. Lett. **110**, 206601 (2013).

[23] N. Vlietstra, J. Shan, V. Castel, B. J. van Wees, and J. Ben Youssef, Spin-Hall magnetoresistance in platinum on yttrium iron garnet: Dependence on platinum thickness and in-plane/out-of-plane magnetization, Phys. Rev. B **87**, 184421 (2013).

[24] C. Hahn, G. de Loubens, O. Klein, M. Viret, V. V. Naletov, and J. Ben Youssef, Comparative measurements of inverse spin Hall effects and magnetoresistance in YIG/Pt and YIG/Ta, Phys. Rev. B **87**, 174417 (2013).

[25] M. Althammer, S. Meyer, H. Nakayama, M. Schreier, S. Altmannshofer, M. Weiler, H. Huebl, S. Geprägs, M. Opel, R. Gross, D. Meier, C. Klewe, T. Kuschel, J.-M. Schmalhorst, G. Reiss, L. Shen, A. Gupta, Y.-T. Chen, G. E. W. Bauer, E. Saitoh, and S. T. B. Goennenwein, Quantitative study of the spin Hall magnetoresistance in ferromagnetic insulator/normal metal hybrids, Phys. Rev. B **87**, 224401 (2013).

[26] N. Vlietstra, J. Shan, V. Castel, J. Ben Youssef, G. E. W. Bauer, and B. J. van Wees, Exchange magnetic field torques in YIG/Pt bilayers observed by the spin-Hall magnetoresistance, Appl. Phys. Lett. **103**, 032401 (2013).

[27] M. Isasa, A. Bedoya-Pinto, S. Vélez, F. Golmar, F. Sánchez, L. E. Hueso, J. Fontcuberta, and F. Casanova, Spin Hall magnetoresistance at Pt/CoFe$_2$O$_4$ interfaces and texture effects, Appl. Phys. Lett. **105**, 142402 (2014).

[28] S. Vélez, A. Bedoya-Pinto, W. Yan, L. E. Hueso, and F. Casanova, Competing effects at Pt/YIG interfaces: Spin Hall magnetoresistance, magnon excitations and magnetic frustration, arXiv:1606.02968.

[29] M. Weiler, M. Althammer, M. Schreier, J. Lotze, M. Pernpeintner, S. Meyer, H. Huebl, R. Gross, A. Kamra, J. Xiao, Y.-T. Chen, H. J. Jiao, G. E. W. Bauer, and S. T. B. Goennenwein, Experimental Test of the Spin Mixing Interface Conductivity Concept, Phys. Rev. Lett. **111**, 176601 (2013).

[30] M. Shreier, N. Roschewsky, E. Dobler, S. Meyer, H. Huebl, R. Gross, and S. T. B. Goennenwein, Current heating induced spin Seebeck effect, Appl. Phys. Lett. **103**, 242404 (2013).

[31] N. Vlietstra, J. Shan, B. J. van Wees, M. Isasa, F. Casanova, and J. Ben Youssef, Simultaneous detection of the spin-Hall magnetoresistance and the spin-Seebeck effect in platinum

and tantalum on yttrium iron garnet, Phys. Rev. B **90,** 174436 (2014).

[32] K. Uchida, J. Xiao, H. Adachi, J. Ohe, S. Takahashi, J. Ieda, T. Ota, Y. Kajiwara, H. Umezawa, H. Kawai, G. E. W. Bauer, S. Maekawa, and E. Saitoh, Spin Seebeck insulator, Nat. Mater. **9,** 894 (2010).

[33] E. Saitoh, M. Ueda, H. Miyajima, and G. Tatara, Conversion of spin current into charge current at room temperature: Inverse spin-Hall effect, Appl. Phys. Lett. **88,** 182509 (2006).

[34] K. Ando, S. Takahashi, K. Harii, K. Sasage, J. Ieda, S. Maekawa, and E. Saitoh, Electric Manipulation of Spin Relaxation Using the Spin Hall Effect, Phys. Rev. Lett. **101,** 036601 (2008).

[35] Y. Kajiwara, K. Harii, S. Takahashi, J. Ohe, K. Uchida, M. Mizuguchi, H. Umezawa, H. Kawai, K. Ando, K. Takanashi, S. Maekawa, and E. Saitoh, Transmission of electrical signals by spin-wave interconversion in a magnetic insulator, Nature (London) **464,** 262 (2010).

[36] E. Villamor, M. Isasa, S. Vélez, A. Bedoya-Pinto, P. Vavassori, L. E. Hueso, F. S. Bergeret, and F. Casanova, Modulation of pure spin currents with a ferromagnetic insulator, Phys. Rev. B **91,** 020403(R) (2015).

[37] F. K. Dejene, N. Vlietstra, D. Luc, X. Waintal, J. Ben Youssef, and B. J. van Wees, Control of spin current by a magnetic YIG substrate in NiFe/Al nonlocal spin valves, Phys. Rev. B **91,** 100404(R) (2015).

[38] J. C. Slonczewski, Origin of magnetic anisotropy in cobalt-substituted magnetite, Phys. Rev. **110,** 1341 (1958).

[39] R. H. Kodama, A. E. Berkowitz, E. J. McNiff, Jr., and S. Foner, Surface Spin Disorder in $NiFe_2O_4$ Nanoparticles, Phys. Rev. Lett. **77,** 394 (1996).

[40] N. Dix, I. Fina, R. Bachelet, L. Fàbrega, C. Kanamadi, J. Fontcuberta, and F. Sánchez, Large out-of-plane ferro-electric polarization in flat epitaxial $BaTiO_3$ on $CoFe_2O_4$ heterostructures, Appl. Phys. Lett. **102,** 172907 (2013).

[41] C. Burrowes, B. Heinrich, B. Kardasz, E. A. Montoya, E. Girt, Y. Sun, Y.-Y. Song, and M. Wu, Enhanced spin pumping at yttrium iron garnet/Au interfaces, Appl. Phys. Lett. **100,** 092403 (2012).

[42] L. Qiu, K. Ando, K. Uchida, Y. Kajiwara, R. Takahashi, H. Nakayama, T. An, Y. Fujikawa, and E. Saitoh, Spin mixing conductance at a well-controlled platinum/yttrium iron garnet interface, Appl. Phys. Lett. **103,** 092404 (2013).

[43] Y. Ando, K. Ichiba, S. Yamada, E. Shikoh, T. Shinjo, K. Hamaya, and M. Shiraishi, Giant enhancement of spin pumping efficiency using Fe_3Si ferromagnet, Phys. Rev. B **88,** 140406(R) (2013).

[44] M. Erekhinsky, F. Casanova, I. K. Schuller, and A. Sharoni, Spin-dependent Seebeck effect in non-local spin valve devices, Appl. Phys. Lett. **100,** 212401 (2012); M. Erekhinsky, A. Sharoni, F. Casanova, and I. K. Schuller, Surface enhanced spin-flip scattering in lateral spin valves, Appl. Phys. Lett. **96,** 022513 (2010).

[45] J. J. Hauser, Magnetic proximity effect, Phys. Rev. **187,** 580 (1969).

[46] W. J. Antel, Jr., M. M. Schwickert, T. Lin, W. L. O'Brien, and G. R. Harp, Induced ferromagnetism and anisotropy of

Pt layers in Fe/Pt(001) multilayers, Phys. Rev. B **60,** 12933 (1999).

[47] S. Geprägs, S. Meyer, S. Altmannshofer, M. Opel, F. Wilhelm, A. Rogalev, R. Gross, and S. T. B. Goennenwein, Investigation of induced Pt magnetic polarization in $Pt/Y_3Fe_5O_{12}$ bilayers, Appl. Phys. Lett. **101,** 262407 (2012).

[48] Y. M. Lu, Y. Choi, C. M. Ortega, X. M. Cheng, J. W. Cai, S. Y. Huang, L. Sun, and C. L. Chien, Pt Magnetic Polarization on $Y_3Fe_5O_{12}$ and Magnetotransport Characteristics, Phys. Rev. Lett. **110,** 147207 (2013); B. F. Miao, S. Y. Huang, D. Qu, and C. L. Chien, Physical Origins of the New Magnetoresistance in Pt/YIG, Phys. Rev. Lett. **112,** 236601 (2014).

[49] J. X. Li, M. W. Jia, Z. Ding, J. H. Liang, Y. M. Luo, and Y. Z. Wu, Pt-enhanced anisotropic magnetoresistance in Pt/Fe bilayers, Phys. Rev. B **90,** 214415 (2014).

[50] M. Valvidares, N. Dix, M. Isasa, K. Ollefs, F. Wilhelm, A. Rogalev, F. Sánchez, E. Pellegrin, A. Bedoya-Pinto, P. Gargiani, L. E. Hueso, F. Casanova, and J. Fontcuberta, Absence of magnetic proximity effects in magnetoresistive $Pt/CoFe_2O_4$ hybrid interfaces, Phys. Rev. B **93,** 214415 (2016).

[51] N. Cusack, *The Electrical and Magnetic Properties of Solids* (Longmans, New York, 1958), Chap. 6, p. 132.

[52] A. B. Pippard, *Magnetoresistance in Metals* (Cambridge University Press, Cambridge, England, 1989).

[53] S. Vélez, V. N. Golovach, A. Bedoya-Pinto, M. Isasa, E. Sagasta, M. Abadia, C. Rogero, L. E. Hueso, F. S. Bergeret, and F. Casanova, Hanle Magnetoresistance in Thin Metal Films with Strong Spin-Orbit Coupling, Phys. Rev. Lett. **116,** 016603 (2016).

[54] F. Rigato, J. Geshev, V. Skumryev, and J. Fontcuberta, The magnetization of epitaxial nanometric $CoFe_2O_4$ (001) layers, J. Appl. Phys. **106,** 113924 (2009).

[55] A. Lisfi, C. M. Williams, L. T. Nguyen, J. C. Lodder, A. Coleman, H. Corcoran, A. Johnson, P. Chang, A. Kumar, and W. Morgan, Reorientation of magnetic anisotropy in epitaxial cobalt ferrite thin films, Phys. Rev. B **76,** 054405 (2007).

[56] D. T. Margulies, F. T. Parker, M. L. Rudee, F. E. Spada, J. N. Chapman, P. R. Aitchison, and A. E. Berkowitz, Origin of the Anomalous Magnetic Behavior in Single Crystal Fe_3O_4 Films, Phys. Rev. Lett. **79,** 5162 (1997).

[57] W. Eerenstein, T. T. M. Palstra, S. S. Saxena, and T. Hibma, Spin-Polarized Transport across Sharp Anti-ferromagnetic Boundaries, Phys. Rev. Lett. **88,** 247204 (2002).

[58] M. Foerster, J. M. Rebled, S. Estradé, F. Sánchez, F. Peiró, and J. Fontcuberta, Distinct magnetism in ultrathin epitaxial $NiFe_2O_4$ films on $MgAl_2O_4$ and $SrTiO_3$ single crystalline substrates, Phys. Rev. B **84,** 144422 (2011).

[59] J.-B. Moussy, S. Gota, A. Bataille, M.-J. Guittet, M. Gautier-Soyer, F. Delille, B. Dieny, F. Ott, T. D. Doan, P. Warin, P. Bayle-Guillemaud, C. Gatel, and E. Snoeck, Thickness dependence of anomalous magnetic behavior in epitaxial Fe_3O_4(111) thin films: Effect of density of anti-phase boundaries, Phys. Rev. B **70,** 174448 (2004).

[60] C. Jin, H. Liu, P. Li, D. F. Kuang, and H. L. Bai, Anomalous magnetic properties of the epitaxial $CoFe_2O_4$ films prepared by reactive cosputtering, J. Appl. Phys. **110**, 013917 (2011).

[61] M. Gich, I. Fina, A. Morelli, F. Sánchez, M. Alexe, J. Gàzquez, J. Fontcuberta, and A. Roig, Multiferroic iron oxide thin films at room temperature, Adv. Mater. **26**, 4645 (2014).

[62] R. G. S. Sofin, S. K. Arora, and I. V. Shvets, Positive antiphase boundary domain wall magnetoresistance in Fe_3O_4 (110) heteroepitaxial films, Phys. Rev. B **83**, 134436 (2011).

[63] C. Gatel, B. Warot-Fonrose, S. Matzen, and J.-B. Moussy, Magnetism of $CoFe_2O_4$ ultrathin films on $MgAl_2O_4$ driven by epitaxial strain, Appl. Phys. Lett. **103**, 092405 (2013).

[64] See Supplemental Material at http://link.aps.org/supplemental/10.1103/PhysRevApplied.6.034007 for a full VSM characterization of the second set of samples.